Cyclic degradation mechanisms in aged FeNiCoAlTa shape memory single crystals

P. Krooß [a,*], C. Somsen [b], T. Niendorf [a], M. Schaper [a], I. Karaman [c], Y. Chumlyakov [d], G. Eggeler [b], H.J. Maier [e]

[a] *Lehrstuhl für Werkstoffkunde (Materials Science), University of Paderborn, 33098 Paderborn, Germany*
[b] *Institut für Werkstoffkunde, Ruhr-Universität Bochum, 44780 Bochum, Germany*
[c] *Department of Materials Science and Engineering, Texas A&M University, College Station, TX 77843, USA*
[d] *Siberian Physical Technical Institute, Tomsk State University, 634050 Tomsk, Russia*
[e] *Institut für Werkstoffkunde (Materials Science), Leibniz Universität Hannover, 30823 Garbsen, Germany*

Abstract

This study focuses on the functional stability of [0 0 1]-oriented $Fe_{41}Ni_{28}Co_{17}Al_{11.5}Ta_{2.5}$ (at.%) single crystals. It is shown that functional degradation of aged FeNiCoAlTa, containing fine dispersed γ'-particles $\sim$5–8 nm in diameter is caused by the interaction of different martensite variants under cyclic loading in tension. Superelastic cycling experiments up to 4.5% total strain resulted in the accumulation of permanent strain mainly caused by the formation of retained martensite. In situ observations were conducted in order to evaluate the local strain evolution and martensite variant interactions on the meso- and microscale. Optical microscopy and transmission electron microscopy observations revealed various differently oriented martensite variants which were retained upon 100 superelastic cycles. In addition, fine martensitic structures remaining in the vicinity of the γ' precipitates were found after mechanical cycling, which are shown to be important for cyclic degradation in Fe-based shape memory alloys.

1. Introduction

Iron-based shape memory alloys (Fe-based SMAs) such as FeMnAlNi and FeCoNiTi have attracted a lot of recent attention due to their better workability and lower processing costs as compared to traditional SMAs such as NiTi [1–7]. Furthermore, most Fe-based SMAs exhibit high theoretical transformation strains, which make them very attractive for superelastic and damping applications [3,7]. Recent developments have shown that the precipitation of the ordered $L1_2$ phase (γ') leads to a change in the martensitic transformation characteristics from non-thermoelastic to thermoelastic [7–9]. It was shown that fine dispersed γ'-precipitates are able to harden the matrix by the formation of coherent stress fields in FeNiCoTi SMAs, resulting in the suppression of dislocation plasticity and, thus, a thermoelastic martensitic transformation and a reduction in temperature hysteresis from several hundred degrees to $\approx$120 °C [6,10]. However, experimental data revealed that most of the Fe-based SMAs that exhibit a face-centered cubic (fcc) to body-centered tetragonal (bct) phase transformation possess very low transformation strains, e.g. FeNiCoTi with only about 2%, as compared to conventional NiTi SMAs [10,11].

* Corresponding author. Tel.: +49 (0) 5251 60 3832; fax: +49 5251 60 3854.
  E-mail address: krooss@lwk.upb.de (P. Krooß).

In a recent study, a FeNiCoAlTa SMA with a fcc to bct transformation showed very high recoverable superelastic strains of up to 13% under tensile loading [7]. Whereas these high superelastic strains have been demonstrated in a textured polycrystalline FeNiCoAlTa SMA in single-cycle tests at room temperature (RT), only 6.8% superelastic strain was reported for the single-crystalline condition under the same loading conditions [9]. These experimentally observed values are well below the theoretically determined maximum transformation strain of 8.7% under tensile loads [7]. The mismatch between the calculated theoretical value and the experimentally observed one is associated with the high volume fraction of non-transforming γ'-precipitates [12,13]. Depending on the heat treatment performed, volume fractions of 20–38% were obtained [8,13].

Several studies have focused on the role of the fine dispersed γ'-particles following different aging heat treatments in FeNiCoAlTa alloys [8,9,11–17]. These particles were intensively characterized by Ma et al. using atom probe microscopy imaging to resolve the precipitates and quantify their size, volume fraction and composition, as well as the decomposition of the matrix in the vicinity of the precipitates [13]. By means of artificial aging, both the size and coherency, i.e. the coherency stress fields, of the particles as well as the chemical composition of the matrix are affected, leading to a shift in transformation temperatures as well as transformation stresses and strains, respectively [12–17].

Considering practical applications, cyclic stability is a crucial performance criterion for SMAs; however, data reporting on the mechanisms governing functional degradation in Fe-based SMAs are rare. For NiTi alloys, it has been found that cyclic degradation is due to the stabilization of martensite induced by dislocation pinning of phase boundaries [18–24]. An increase in dislocation density, finally leading to transformation strain irreversibility, results from several microstructural mechanisms, e.g. microplasticity due to locally low matrix strength and phase boundary friction [18–24]. Increase in the strength of the matrix induced by grain refinement in polycrystalline NiTi alloys [25] or introduction of optimized precipitates has been shown to result in significant improvement of cyclic stability [18,26]. Clearly, considering precipitates, it is still difficult to accurately weight the contribution of each factor on the martensitic transformation. Precipitates, on one hand, lead to a change in the chemical composition of the alloy matrix and, thus, affect the phase stability and eventually the driving force for phase transformation. On the other hand coherency stresses are introduced, leading to matrix strengthening and decrease of transformation stress [12–14,16–19,26]. As a consequence, not only the volume fraction and size determines the SMA behavior, but the shape of the precipitates and the kind of stress field linked thereto has also to be accounted for [13,16,17,27].

Due to the complex nature of dislocation slip–martensite variant–precipitate phase stability interactions in SMAs, the role of each mechanism contributing to the cyclic degradation in Fe-based SMAs cannot yet be deduced from data available in literature. In a recent study, it was shown that variation in particle size significantly affects the cyclic transformation behavior in FeNiCoAlTa SMAs and a reduction in particle size results in an improvement in cyclic stability [16]. The present study focuses on the tensile cyclic deformation behavior of [0 0 1]-oriented FeNiCoAlTa SMA single crystals aged for 1 h at 700 °C in order to investigate the microstructural features affecting the cyclic phase transformation behavior and evaluate their impact on cyclic degradation mechanisms. In situ optical microscopy (OM) and post-mortem transmission electron microscopy (TEM) were carried out in order to shed light on the microstructural features that govern functional degradation and defect generation.

2. Materials and experimental techniques

Ingots of FeNiCoAlTa with a nominal composition of $Fe_{41}Ni_{28}Co_{17}Al_{11.5}Ta_{2.5}$ (at.%) were produced using vacuum induction melting. The single crystals were grown using the Bridgman technique in a helium atmosphere. Dog-bone-shaped samples with a gauge length of 8 mm and a cross section of 1.6 mm × 1.5 mm were machined from the bulk material with the [0 0 1] orientation parallel to the loading direction.

Homogenization of the samples was done at 1300 °C for 24 h and the samples were water-quenched (WQ) followed by an aging heat treatment for 1 h at 700 °C under argon atmosphere to produce fine coherent γ'-$(Ni,Fe,Co)_3(Al,Ta)$ precipitates. During homogenization, the samples were kept in evacuated quartz glass tubes in order to avoid oxidation during the solution heat treatment.

In situ superelastic cycling experiments were performed using a servohydraulic test frame in displacement control mode with a fixed maximum strain upon loading and a minimum stress for unloading. Strains were measured using a miniature extensometer attached directly to the gauge length of the sample. In situ OM was performed using a digital microscope mounted in front of the specimen. Confocal laser scanning microscopy (CLSM) with a 408 nm violet laser was employed simultaneously for single-cycle tests with the samples mounted in a miniature load frame. The CLSM used is equipped with a 408 nm violet laser. The OM images were taken at a given number of cycles in the load-free condition, i.e. after the 1st, 50th and 100th cycles, to evaluate the evolution of local irreversible strains. For calculation of strain fields, the digital image correlation (DIC) technique was employed using a subset size of 41 pixels × 41 pixels and a stepsize of 3 pixels.

High resolution transmission electron microscopy (HR-TEM) analyses were conducted using a FEI Tecnai F20 operating at 200 kV. For the TEM sample preparation two different techniques were used. For electrochemical preparation, the specimens were first mechanically ground and polished down to a thickness of 0.15 mm. Finally electron-transparent areas were obtained using twin-jet
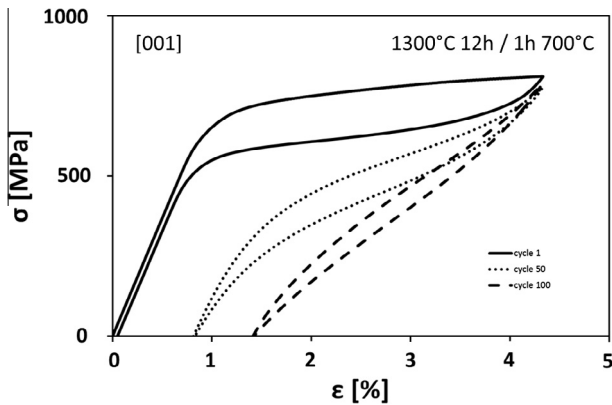
Fig. 1. Cyclic stress–strain response of an [001]-oriented $Fe_{41}Ni_{28}Co_{17}Al_{11.5}Ta_{2.5}$ (at.%) single crystal cycled in tension at room temperature.

polishing with a solution of 600 ml methanol, 340 ml butanol and 60 ml perchloric acid under an applied potential of 70 V at a temperature of −25 °C. In addition, focused ion beam (FIB; Quanta 200 3D) TEM sample preparation was used for microstructural characterization of a predefined position and lamellae were taken out of the area of interest (AOI) of the fatigued samples.

3. Results and discussion

3.1. Characterization of the cyclic stress–strain response

In order to identify the mechanisms governing functional degradation during cyclic transformation of $Fe_{41}Ni_{28}Co_{17}Al_{11.5}Ta_{2.5}$ (at.%) single crystals, superelastic cycling experiments at room temperature were carried out. Excellent superelasticity was observed in the first cycle at room temperature (Fig. 1). However, in the very first cycles functional degradation set in. Fig. 1 demonstrates the pronounced functional degradation which is macroscopically manifested by the shake-down in the critical stress (σ_{crit}) for the stress-induced martensitic transformation (SIMT), the accumulation of permanent strain and a decrease in stress hysteresis. Microstructural changes leading to functional degradation are often attributed to the formation of residual, retained martensite induced by conventional plasticity, i.e. dislocation slip, which is supposed to be connected to the martensitic phase front propagation within the austenitic parent phase [18,19,22]. As dislocation slip is partly irreversible, unloading is not sufficient for a complete shape restoration. Moreover, dislocations interact with the initially easily propagating martensite/austenite phase boundaries in such a way that some of these boundaries are pinned [22,28]. Consequently, retained martensite evolves steadily during cycling.

Starting from a σ_{crit} for SIMT at ≈740 MPa in the 1st cycle, σ_{crit} decreases to nearly 400 MPa by cycle 50 and to ≈150 MPa by cycle 100 (cf. Fig. 1). Additionally, permanent strain increases following each cycle up to about 1.4% in cycle 100. Furthermore, the stress hysteresis is affected significantly during cyclic loading, showing a decrease from 150 MPa in the 1st cycle to 100 and 60 MPa in the 50th and 100th cycles, respectively. It is assumed that the frictional energy at the austenite–martensite phase boundaries may
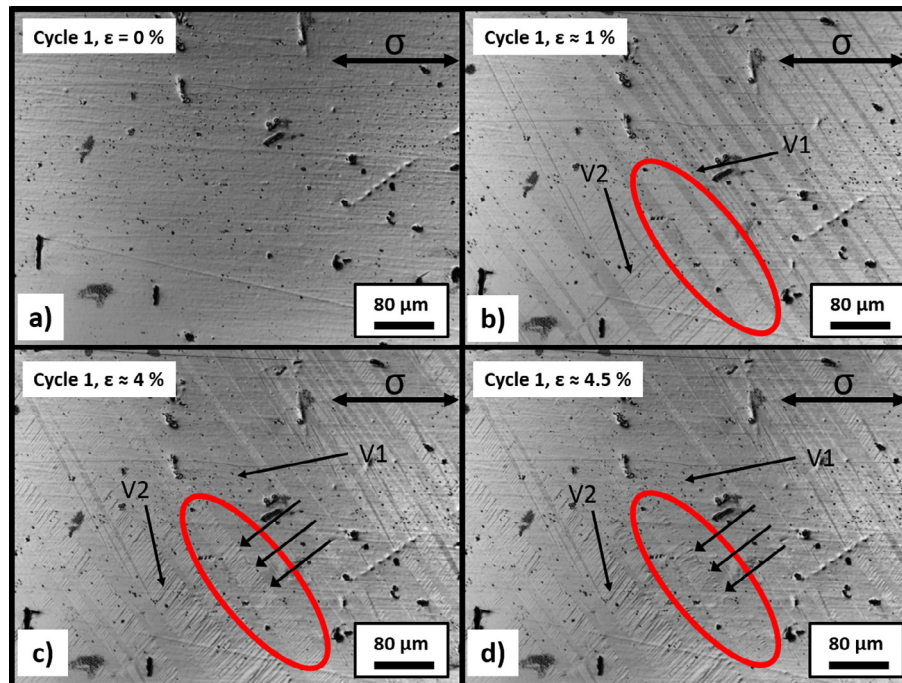

Fig. 2. In situ observation of the surface evolution during the phase transformation of an [001]-oriented $Fe_{41}Ni_{28}Co_{17}Al_{11.5}Ta_{2.5}$ (at.%) single crystal under tension within the first cycle. (a) indicates the initial condition before the onset of the martensitic transformation, (b) was recorded at 1%, (c) at 4% and (d) at 4.5% global strain. The oval markings indicate the area of interest and the three arrows highlight the apparent interaction zone of different martensite variants.
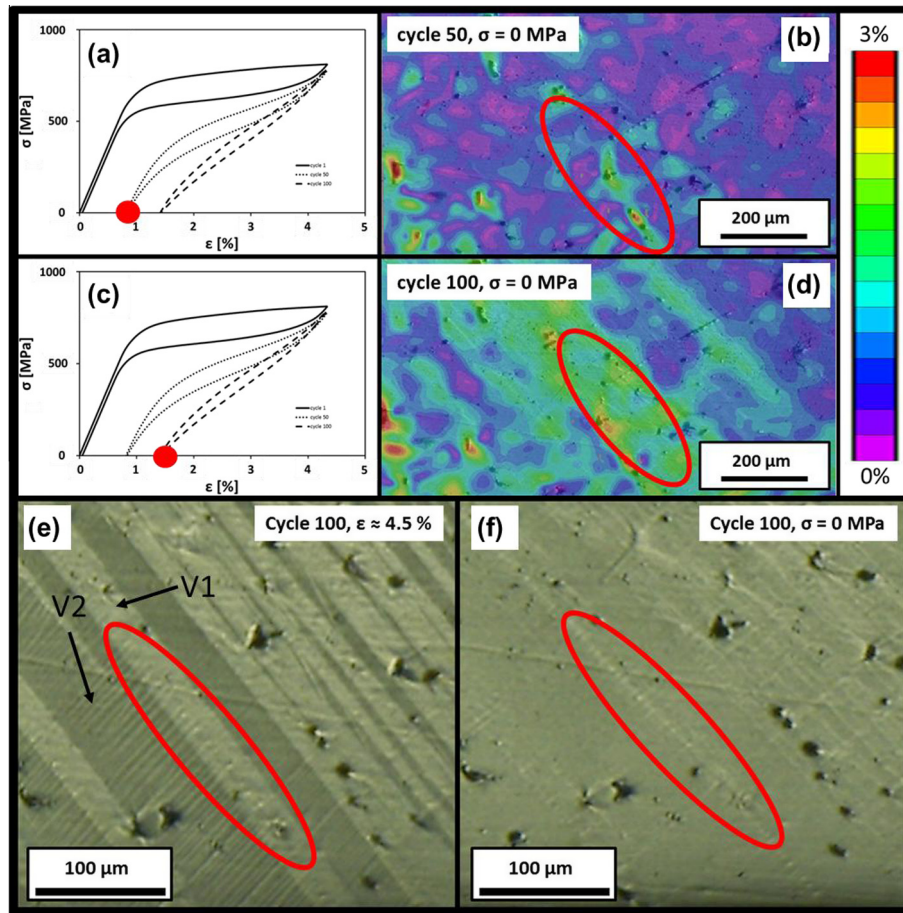
Fig. 3. In situ observation of the cyclic deformation as observed by in situ DIC and in situ OM. The red dots in (a) and (c) indicate the state of deformation. (b) and (d) show the corresponding local strains from in situ DIC observations. (e) illustrates the in situ OM at 4.5% strain and (f) the stress-free condition after cycle 100. The oval markings highlight the areas where variant interactions were most prominent on the sample surface. (For interpretation of the references to colour in this figure legend, the reader is referred to the web version of this article.)

lead to an increased dislocation activity [18,19,22]. Thus, considering conventional degradation mechanisms, the formation of residual martensite may be connected to a higher dislocation activity at the austenite–martensite phase boundaries as small stress fields of the dislocations are capable of pinning the martensite variants that have evolved under load [22]. In fact, Simon et al. showed in their study that dislocation arrangements remained after a superelastic in situ TEM experiment, providing the mechanical energy required to retain the stress-induced martensite.

Depending on the number of martensite variants activated, there are, however, at least two scenarios resulting in an increased dislocation activity in most of the conventional SMAs and probably also in FeNiCoAlTa SMAs. Firstly, the SIMT can activate only a single martensite variant. In this case, assuming that the hardness of the parent phase is fairly low, an increased dislocation activity at the austenite–martensite interphase occurs, leading to local and global strain accumulations due to plasticization and the formation of pinned martensite [18,19,22]. These regions containing a high amount of pinned martensite are stabilized in the austenitic matrix at temperatures well

above the austenite finish (A_f) as the stress fields of the dislocations provide the mechanical energy necessary to retain the martensite phase [29].

Secondly, the SIMT may occur by activating multiple martensite variants. In this case different martensite variants could interact and lead to a higher dislocation activity at the phase boundaries of the interacting martensite variants. The impact of this process on both the superelastic and the shape memory properties was investigated intensively in several studies [13,28,30–32]. Dadda et al. showed that the activation of multiple martensite variants does lead to an increased stress hysteresis and a pronounced cyclic degradation in CoNiGa SMAs [28,30–32]. They attributed this to the formation of at least two differently oriented martensite variants, resulting in an increased dislocation activity at the interface. In another study Ma et al. reported that a single variant is activated in compression, while tensile loads resulted in multi-variant activation in the [001]-oriented FeNiCoAlTa shape memory single crystals [13]. They also demonstrated that the single-variant activation under compressive loads leads to irrecoverable transformation due to incompatibilities at the austenite–martensite interface due to the lack of detwinning in FeNiCoAlTa

SMAs under compression [13]. By contrast, internal twinning is promoted under tensile loads because of a preferential activation of at least two martensite variants. This leads to a higher compatibility at the austenite–martensite interface due to the favored formation of corresponding variant pairs (CVPs) [13]. Similarly, multi-variant activation seems to be prevalent in the present study. Specifically, the high degree of recoverability in the first cycle indicates internal detwinning as the favored accommodation process under tension, which in turn suppresses pronounced irreversible processes. Although, internal twinning and detwinning is a beneficial feature, it seems to dominate only in the case of single-cycle experiments. Clearly, irreversible deformation, i.e. the accumulation of permanent strain, sets in after a few cycles (Fig. 1).

The in situ tests conducted in the present study revealed localized deformations, as discussed in more detail in the next section. The decrease in stress hysteresis with increasing number of superelastic cycles is mainly due to the formation of retained martensite variants. This leads to further decrease in stress hysteresis in the subsequent cycles due a decreased transformation strain in the experiments with a constant strain end point (Fig. 1).

3.2. In situ observations

In order to uncover the mechanisms that govern cyclic degradation in FeNiCoAlTa SMAs, in situ single-cycle and cyclic tests were conducted. Fig. 2 shows the evolution of the sample surface within the 1st cycle, which is an indicator of the ongoing phase transformation. These data were obtained using high-resolution CLSM. The martensite phase is represented by the darker grey areas because of its lower CLSM intensity signal due to its slightly distorted character. With increasing stress level the sample surface exhibits at least two different martensite variants oriented under 55°, 135° to the loading direction for the martensite variants marked V1 and V2. This is in good agreement with the results of Ma et al. who postulated multivariant activation under tensile loads [13]. With increasing deformation, the martensite variants grow in width (Fig. 2b–d) until both variants start to interact at ≈1% global strain. At the maximum macroscopic strain level of 4.5%, local distortion at the interphase boundaries becomes visible (Fig. 2d) as indicated by the three parallel black arrows. However, the SIMT is not completed at this point as some austenitic areas remain untransformed (lighter grey structures in Fig. 2d). Some areas of the specimens are more distorted following the phase transformation (oval marking in Fig. 2d) because of variant interactions, while others show homogeneous single-variant transformation, e.g. the ones containing only the martensite variant V1. The three parallel arrows in Fig. 2c and d highlight the areas of intense variant interaction. It is obvious in Fig. 2c–d that V1 overlaps V2, which results in the aforementioned local distortion.

Fig. 3 shows in situ DIC observations made during the 50th and 100th cycle. The red dots in Fig. 3a and c indicate the actual loading condition and the level of global residual strain. In order to focus on the accumulation of local permanent strain due to defect generation, which is an appropriate measure to evaluate functional stability in SMAs, DIC measurements in the stress-free condition were conducted to identify local strain accumulations on the sample surface corresponding to the macroscopic strain evolution visible in Fig. 1. From Fig. 3b it is apparent that in the
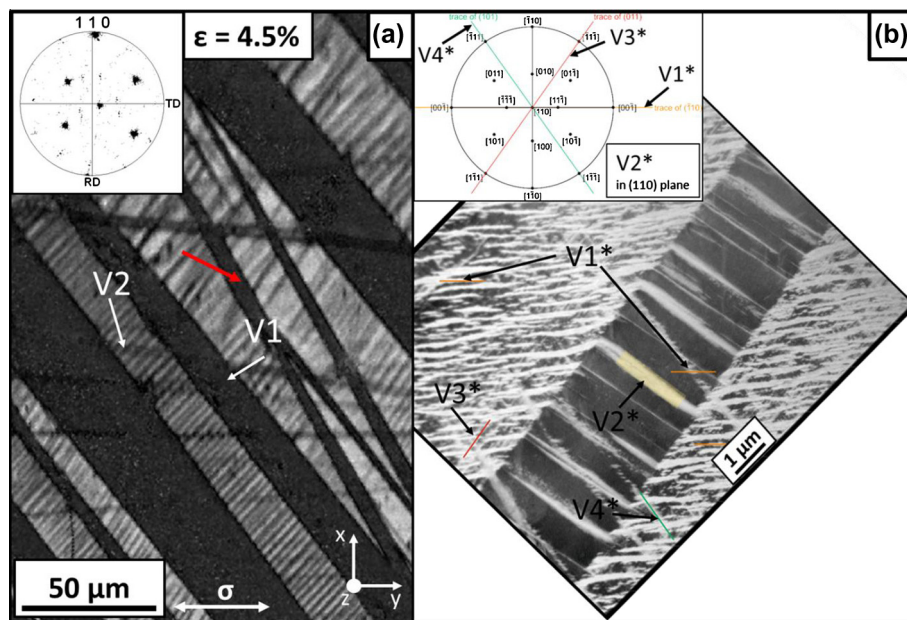

Fig. 4. In situ EBSD observation (a) and post-mortem TEM observation of the electrolytically prepared sample (b) showing similar structures at different magnifications. The loading axis was horizontal in the in situ EBSD experiment of (a) and the TEM image in (b) has been rotated correspondingly. A trace analyzis reveals that the long axes of the martensite variants are located on {110}-type planes.

50th cycle a small amount of local permanent strain is accumulated in some areas. After 100 cycles this has increased significantly (red oval areas in Fig. 3b and d). Clearly, the in situ DIC measurements hint at areas that are more prone to cyclic degradation, which defined the AOI for the subsequent TEM analysis described below.

In Fig. 3, the lighter grey structures represent the martensite phase as it evolved directly from the darker structure, i.e. fcc austenite in the OM micrographs. Again, it is obvious that at least two different martensite variants interact intensively, which are oriented at 80° to each other (Fig. 3d and e). After 100 superelastic cycles at room temperature, the OM in Fig. 3e reveals a surface relief remaining in the stress-free condition. Note that this is the same area that had shown increased local residual strains in the DIC analysis. Thus, the repeated interaction of the martensite variants seems to accumulate defects, which lead to microscopically visible distortion. This is also substantiated by the in situ CSLM single-cycle observation shown in Fig. 2, which did not reveal any defects after unloading in the first cycle. Thus, the cyclic in situ observations clearly point at the local distortional energies in the vicinity of multivariant interactions during cyclic loading significantly affecting the cyclic stability in the [0 0 1]-oriented FeNiCoAlTa SMAs.

3.3. TEM observations

In order to gain better insight into the microstructural mechanisms leading to the observed cyclic degradation of FeNiCoAlTa single crystals, FIB sample preparation was used within the predefined AOI identified via in situ DIC (Fig. 3d and f). As has been shown above, the mechanisms present led to the evolution of permanent strain, which is manifested in both the macroscopic stress–strain response (Fig. 1) and the microscopic, i.e. the local, deformation behavior as evidenced by the in situ DIC and the in situ OM results (Fig. 3).

It is known that FIB sample preparation might lead to an inadvertent heat flow into the samples capable of changing microstructural features such as dislocation arrangements [33]. Thus, a companion part of the specimen was used for conventional electrolytic sample preparation to avoid misinterpretation due to possible artefacts resulting from FIB sample preparation. From Fig. 4 it is obvious that the microscale structures observed in the in situ electron backscattered diffraction (EBSD) experiment (Fig. 4a) look very similar to the nanoscale structures observed in the scanning TEM (STEM) observations (Fig. 4b). Note that the z-axis defined in the Fig. 4a corresponds to the $(1 1 0)$ plane in Fig. 4b. Using lattice parameters reported in a study by Tanaka et al. [5], i.e. $a_0 = 0.3604$ nm for the fcc structure and $a = 0.2771$ nm and $c = 0.3069$ nm for the bct phase, the light grey structures in Fig. 4a can be indexed as the fcc austenite and the darker structures as bct martensite. To allow for better comparability between EBSD and STEM data, EBSD

results have been plotted in the form of an image quality (IQ) map. This is feasible since the bct martensite phase offers lower diffraction intensity because of its highly distorted character.

The corresponding EBSD measurements were conducted in situ at the maximum macroscopic strain level of ≈4.5%. The in situ EBSD measurement clearly illustrates two participating variants (V1 and V2). The red arrow highlights another structure which is supposed to belong to V1. From the in situ results shown in Fig. 2 at least two distinct martensite variants (V1 and V2) formed in the 1st cycle. Their interaction led to significant distortions after 100 cycles (Fig. 3). This is also evident from the post-mortem STEM results (Fig. 4). The STEM image in Fig. 4 was taken from the electrolytically prepared sample, and rotated to correspond to the [0 0 1] loading direction in the in situ images shown in Figs. 2, 3 and 4a. The strong contrasts visible in the STEM image hint at the existence of martensite variants pinned by an increased dislocation activity during cyclic mechanical loading. Note that a
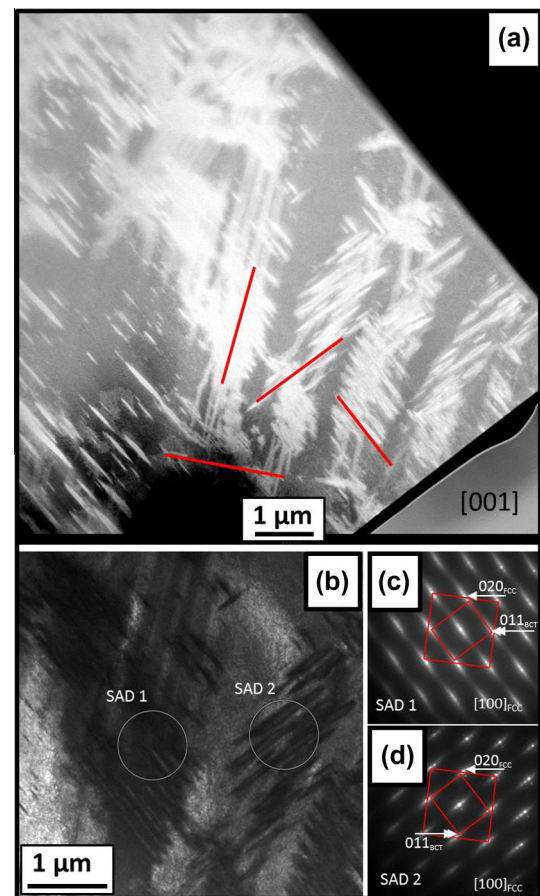

Fig. 5. TEM results of a fatigued FeNiCoAlTa sample after 100 superelastic cycles. (a) shows the results of a STEM investigation on the FIB prepared lamella in the [0 0 1] zone direction, indicating differently oriented high-contrast areas, which could be indexed as bct martensite. The lines denote the four martensite variants. (b) shows the corresponding bright-field image illustrating the position of the two SAED patterns identifying different martensite variants in the reflection spots in (c) and (d), respectively.
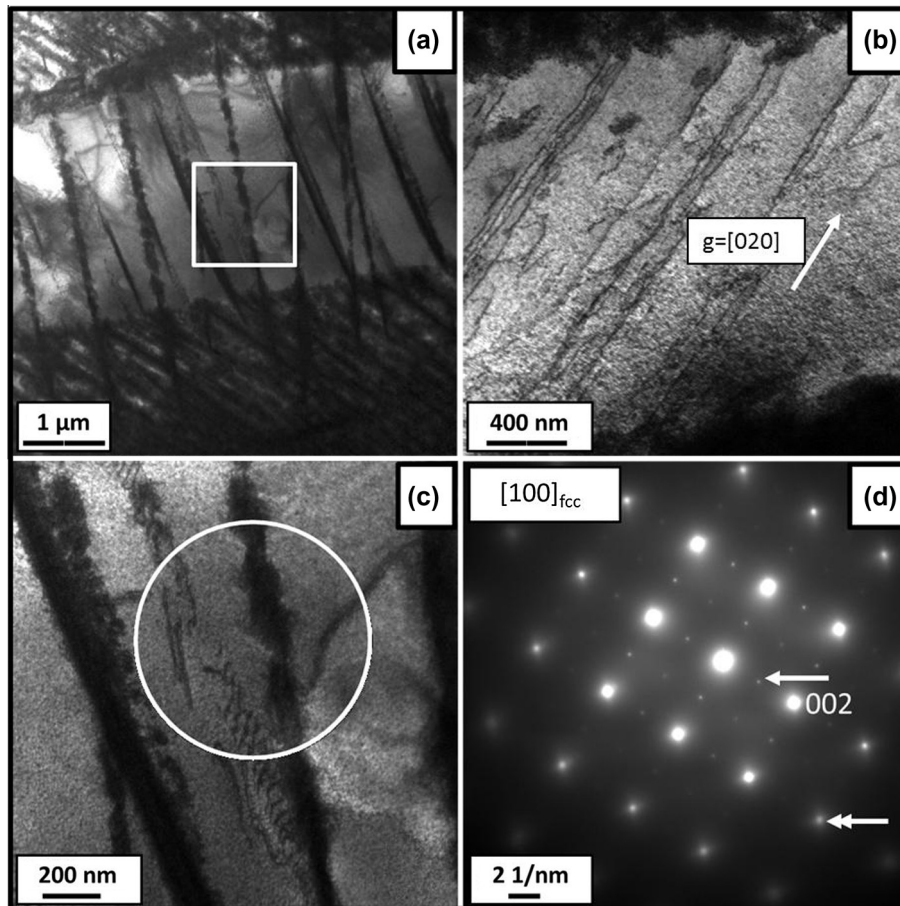
Fig. 6. TEM results from another area of the sample after electrolytic sample preparation. (a) gives an overview showing both retained martensite and dislocation arrangements. (b) was tilted to highlight the dislocation arrangements in the vicinity of the retained martensite variants under a higher magnification. (c) is another higher magnification view from the area marked in (a). The white circle indicates the position of the SAED. The corresponding SAED taken from the 100 pole (d) shows the (0 0 2) reflection spots of the γ'-precipitates indicated by the single arrow. The double arrow highlights a reflection spot exhibiting streaking, indicating the presence of retained martensite.

precise assignment of the martensite variants in Fig. 4a to those in Fig. 4b is difficult because of the different magnifications. However, the impact on the cyclic stability remains unaffected. The traces of the four martensite variants located on {1 1 0}-type planes are marked as V1*, V2*, V3* and V4* in Fig. 4b. This is in good agreement with the in situ results discussed above. The in situ CLSM images (Fig. 2), the in situ EBSD IQ scan (Fig. 4a) and the post-mortem STEM image (Fig. 4b) all reveal that at least two nanoscale martensite variants evolved simultaneously upon mechanical loading. This becomes most obvious from the contrast changes visible in Fig. 4b.

In order to be able to critically discuss the mechanisms leading to localized degradation, a FIB lamella was taken from the AOI defined by the in situ DIC results. This sample was sectioned on a (0 0 1) plane (foil normal of the FIB-lamella parallel to [0 0 1]) in order to analyze the prevailing microstructure and the martensite variants. As is obvious from Fig. 5a, the STEM overview image reveals four different martensite variants partly overlapping each other. Again, it should be noted that for the FIB lamella the electron beam is parallel to the [0 0 1] direction while in Fig. 4b

following electrolytical sample preparation the electron beam is parallel to the [1 1 0] direction. From Fig. 5b two selected-area electron diffraction (SAED) patterns were taken, proving the occurrence of at least two different martensite variants in a highly interacting manner. A third and fourth variant is marked on the traces of the {1 1 0} planes in Fig. 5a, but well-defined reflection spots could not be recorded because they are not located in the [0 0 1] zone axis. The lattice reflection spots taken from the [0 0 1] pole in Fig. 5c and d reveal that all variants evolved on the {1 1 0} planes, which was postulated previously in another study [12,13].

Although the single cycle in situ EBSD results (Fig. 4a) had indicated complete disappearance of the bct martensite variants upon unloading, the TEM image shows a large amount of retained martensite after the superelastic cycling experiment, i.e. following 100 cycles (Fig. 4b). The wider martensite bands visible in the TEM image obviously contain a second martensite variant (marked as V3*) oriented lengthwise, which was not observed in the EBSD image quality scan due to the limited resolution of the EBSD system. V1 visible in the in situ EBSD (Fig. 4a) results and the
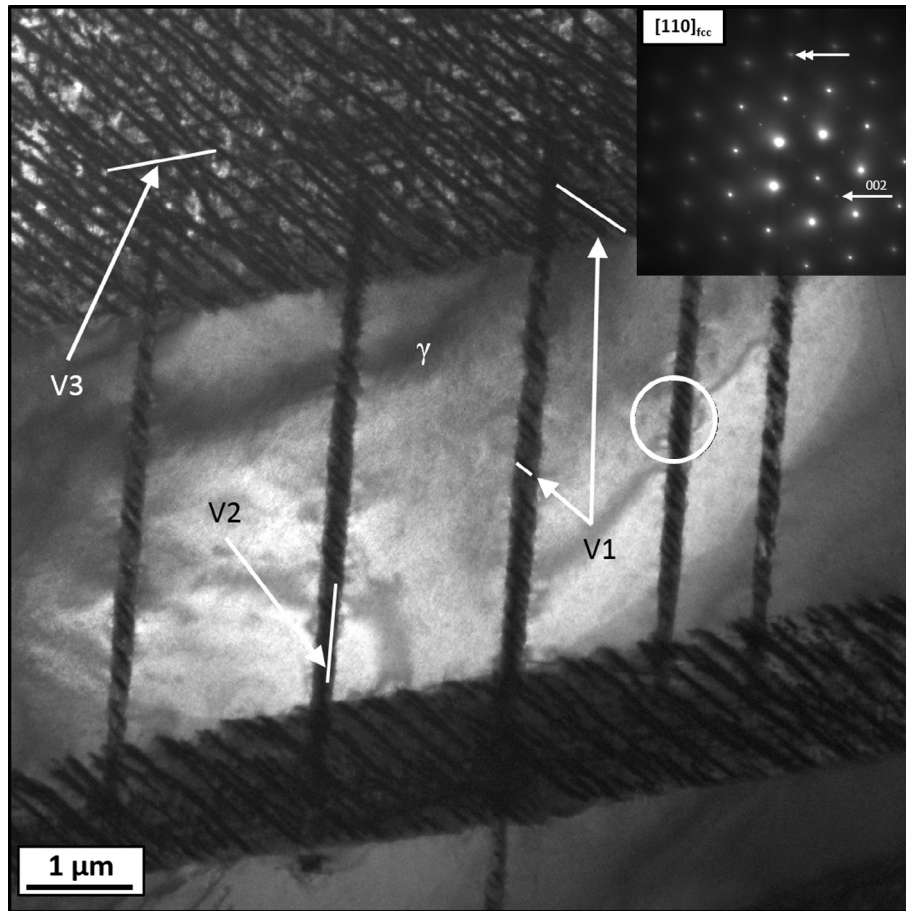
Fig. 7. Bright-field image of the electrolytically prepared sample after 100 superelastic cycles. The white arrows in the bright-field image highlight the different martensite variants within an austenitic matrix. The white circle indicates the position of the SAED taken from the (1 1 0) plane, which is shown in the inset on the upper right. The double arrow marks reflection spots exhibiting streaking, indicating the presence of retained martensite, while the single arrow indicates the (0 0 2) reflection of the γ′-precipitates.

CLSM results (Fig. 2) and the multi-variant band V1* and V3* are defined as V1/V3 in the following. From Fig. 2 it becomes obvious that V2 appears almost at the same stress as does V1/V3. In any case, the three martensite variants remained in an interlocked, pinned condition after 100 cycles. This can be attributed to intense martensite variant interactions, resulting in an increased formation of dislocations introducing localized stress fields capable of retaining the different martensite variants [16,29,32].

In this respect, Fig. 6 highlights that an increased dislocation density is present in the electrolytically prepared sample in the vicinity of retained martensite, proving that this mechanism plays a major role in the observed cyclic degradation. Fig. 6a gives an overview of martensite variant traces. The STEM images, Figs. 4b and 6a, show a large amount of high-contrast structures and scattered dislocation arrangements which can be related to the existence of retained martensite. Fig. 6c illustrates an enlarged area, marked by the white square in Fig. 6a, containing dislocations responsible for the high contrasts in Figs. 4b, 5a, 6a–c and 7. In the SAED taken from the [1 0 0] pole within the area in the white circle in Fig. 6c, the γ′ precipitates become visible as indicated by a white single arrow. In addition,

faint streaking is observed as indicated by the double arrow in Fig. 6d. This can be interpreted as an indication of the existence of a small amount of residual martensite in this area [34]. In order to increase the contrast for a better visualization of dislocation arrangements, the sample was tilted according to the information provided in the micrograph. As shown in Fig. 6b, a large number of dislocation lines between the two multivariant martensite bands visible in Fig. 6a can be deduced. This clearly substantiates the correlation between martensite variant interactions and the increased formation of dislocations, which is supposed to be responsible for the cyclic degradation shown macroscopically in Fig. 1 and was also shown on the mesoscale in the in situ experiments (Figs. 2d and 3f).

In order to further reveal the nature of the martensite variants present, additional TEM analyses have been conducted. The TEM results shown in Fig. 7 reveal that martensite variant V2* contains a small amount of martensite variant V1* when the orientation relationships are taken into account as indicated by high-contrast areas marked by the superimposed white arrows and white lines. In the following, the interaction of V1* and V2* is defined as V1*/V2*. This finding supports the presence of the three
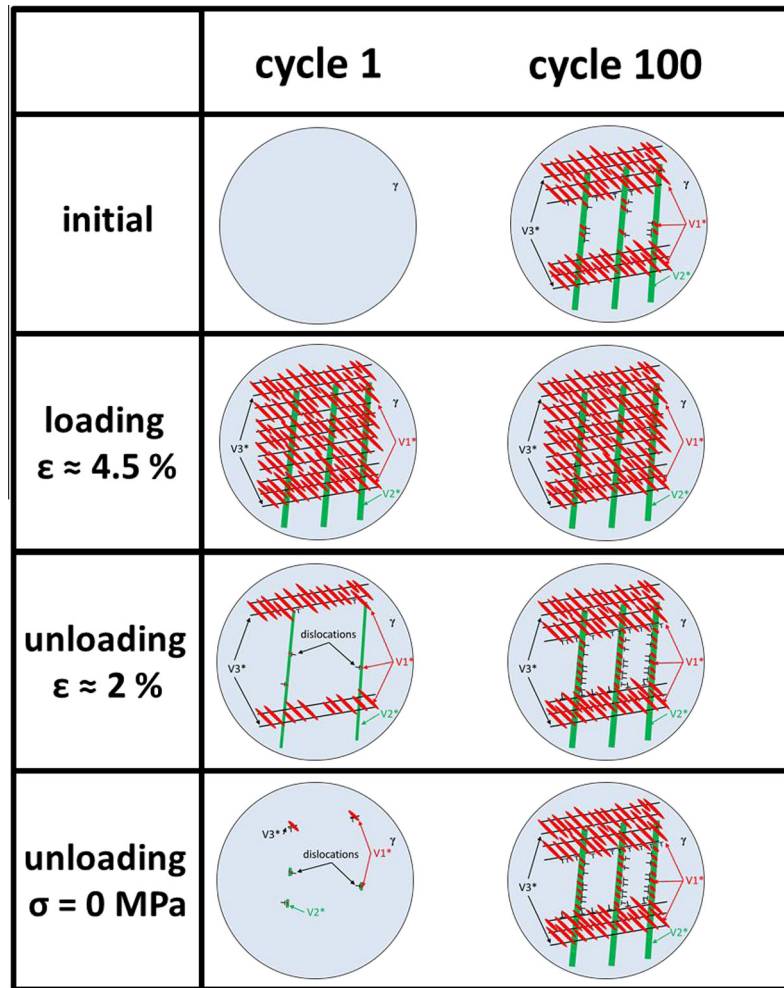
Fig. 8. Schematic detailing the phase transformation in the 1st cycle and after 100 cycles, illustrating the mechanisms that are assumed to be responsible for the observed cyclic degradation.

martensite variants already highlighted in Figs. 4 and 5. Again, high contrasts are supposed to be related to the existence of retained martensite variants induced by an increased dislocation density in their vicinity. As suggested in several studies, martensite variant interactions, and thus increased frictional energies, should result in an intensive pile-up of dislocations in the vicinity of the austenite–martensite phase boundaries due the repeated frictional energy dissipation at the phase boundaries [16,22,30–32]. As discussed above, an increase in the macroscopic strain upon loading results in a considerable distortion at the phase boundaries of at least two different martensite variants (multivariant band V1*/ V3* and V2*) leading to interlocking.

Based on the above post-mortem TEM results, a model illustrating the mechanisms accountable for the cyclic degradation can be proposed. Fig. 8 shows the cyclic degradation model developed for [0 0 1]-oriented FeNiCoAlTa single crystals. The initial condition of the specimen is fully austenitic (Fig 8). Upon loading, three martensite variants evolve and interact with each other, as is obvious from the in situ observations in Fig. 2d at the maximum strain level of 4.5%. At maximum strain, it can be seen that V1/V3

grows at the expense of V2, resulting in distinct distortions at the interfaces. Upon unloading, a few dislocations remain in the austenitic phase, which are capable of stabilizing a very small amount of martensite even after the first superelastic cycle. This is in good agreement with Fig. 1 in which even after the first cycle a small amount of residual strain was observed. Considering a higher number of cycles, this mechanism leads to a substantial increase in dislocation density in each cycle, resulting in a stabilized microstructure containing a large amount of mechanically pinned martensite after 100 cycles (Fig. 7). The proposed model suggests that martensite V2* forms simultaneously with the growth of V1*/V3*. As already discussed, it is also possible that V2* evolves from the austenitic matrix primarily containing a small amount of martensite variant V1*. Nevertheless, the degradation would evolve in a similar fashion. Martensite variants V2* and V3* may also impede each other so that martensite variant V1* is the most favored variant for accommodating macroscopic strains upon loading parallel to the [0 0 1] direction.

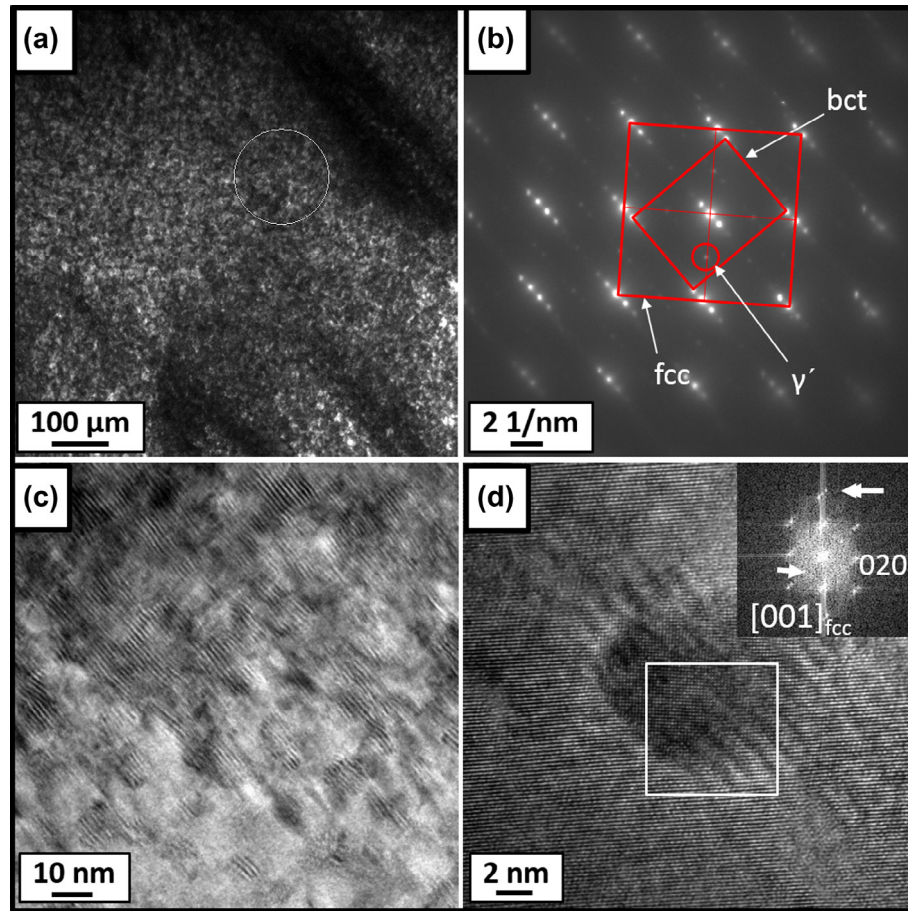The impact of finely dispersed γ′-particles on the cyclic stability of [0 0 1]-oriented FeNiCoAlTa single crystals

Fig. 9. TEM micrographs of the FIB-prepared sample showing the γ'-precipitates. (a) shows a dark-field image. The white circle indicates the position of the SAED shown in (b). The reflection spots in (b) reveal the presence of the fcc phase, the bct phase and the γ'-phase within the apparently two-phase matrix. (c) shows a bright-field image illustrating the size and distribution of the γ'-precipitates featuring a large amount of periodicities at the particles. (d) shows the FFT investigation in the vicinity of a γ'-particle demonstrating the presence of both γ' and bct martensite phases. The arrow indicates {1 1 0}-type reflections of γ'-precipitates and the double arrow marks the reflections due to the bct martensite phase in the vicinity of the particle.

needs to be studied separately. TEM investigations on the sample prepared by FIB (foil normal parallel to [0 0 1] loading direction) revealed that finely dispersed ordered particles seem to affect the cyclic degradation as well as the interaction of the three different martensite variants. The reflection spots in Fig. 9b, corresponding to the circle in Fig. 9a, reveal a bct structure within an fcc austenitic parent phase. The small reflection spots between the main reflection spots of the fcc austenite and bct martensite indicate the presence of the fine ordered γ'-particles. Additional reflection spots are supposed to be due to double diffraction of the fcc parent phase. Fig. 9c and d show HR-TEM images illustrating the size and distribution of the γ'-precipitates. The distribution obtained from Fig. 9c gives reason to assume that the volume fraction of the fine precipitates is be very high as the interparticle distances are less than the particle diameter, which is $\approx$8–10 nm, i.e. somewhat larger than that given by Ma et al. [13]. However, the effect of precipitate size on the superelastic transformation behavior as well as on the cyclic degradation of FeNiCoAlTa SMAs was addressed in a related study [16]. Krooß et al. showed that smaller precipitates following

shorter aging times result in an enhanced cyclic stability. Following this, an optimized heat treatment (1 h at 700 °C) was chosen for this study. Fig. 9c also clearly points out that the precipitates are cluttered with a periodic structure. Higher magnification in combination with FAST Fourier transformation (FFT) revealed the presence of martensite in the immediate vicinity of the precipitates. The FFT image shows reflection spots of the γ'-phase indicated by a single arrow and the martensitic phase indicated by the double arrow within an austenitic matrix. However, TEM investigations of only aged [0 0 1]-oriented FeNiCoAlTa samples showed no residual martensite prior to loading in the vicinity of the γ'-precipitates (not shown here). Thus, it is obvious that the fine martensitic structures in the vicinity of the particles result from the external mechanical load applied during the cycling experiments in this study. This indicates that γ'-particles have a substantial impact on the cyclic degradation behavior as a substantial amount of martensite can be retained in the vicinity of the precipitates. Assuming that the volume fraction of the non-transforming γ'-precipitates is $\approx$38% [13], the estimated maximum transformation strain is $\approx$5.2%.
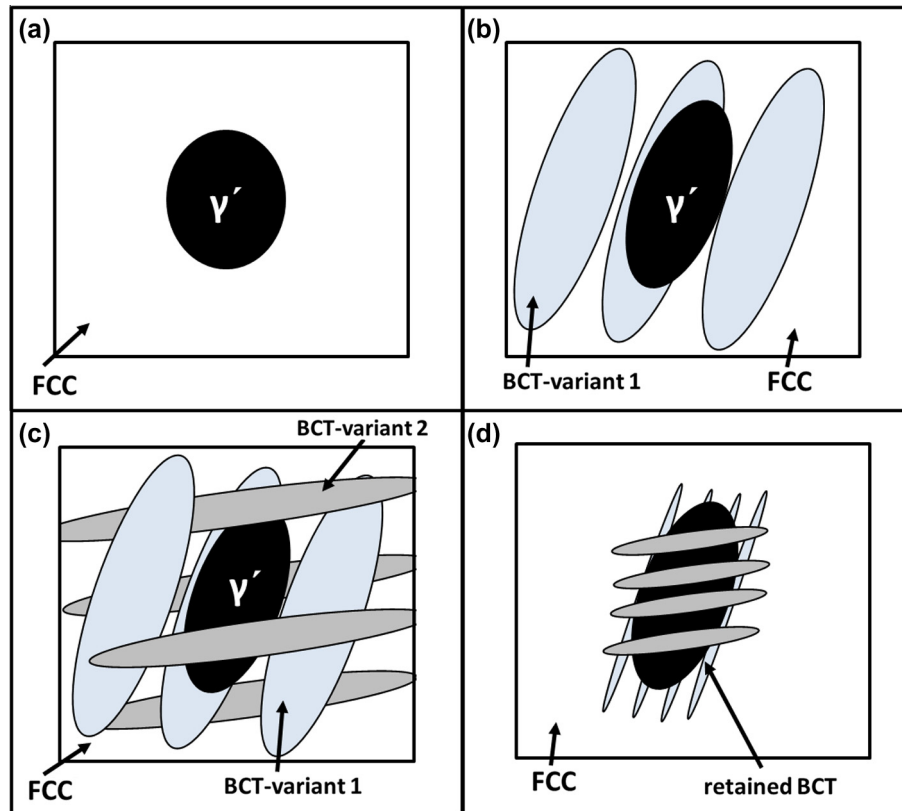
Fig. 10. Schematic illustrating the interaction between evolving martensite variants and precipitates: (a) shows the parent fcc matrix containing γ′-precipitates; (b) illustrates the elastically deformed particle during phase transformation in case of a single martensite variant evolving; (c) illustrates the deformation of the particle in the case of a martensite–variant interaction leading to double shear of the precipitate. (d) represents the unloaded condition after a superelastic cycle, exhibiting retained martensite.

Most of the precipitates are accompanied by residual martensite following 100 superelastic cycles. Taking into account the high volume fraction of precipitates, this mechanism can contribute significantly to the evolution of irreversible strain seen in Fig. 1. It should be noted that a volume fraction of 38% was determined for a heat treatment at 600 °C, and thus the volume fraction is assumed to be somewhat different following the heat treatment of 1 h at 700 °C used in the present study [16,17].

It is not yet clear whether the repeated phase transformation or the initially applied load in the first cycle leads to the formation of retained martensite in the vicinity of the particles. Furthermore, a clear conclusion which mechanism, i.e. the interaction of the martensite variants or the precipitate–martensite interaction, is dominant cannot be convincingly drawn. However, there are at least three possibilities that might account for the presence of retained martensite next to the precipitates. Firstly, the small stress fields of the particles can provide the necessary mechanical energy for retaining martensite variants equivalent to σ_{crit} for SIMT. Secondly, matrix hardness is not sufficient to suppress dislocation motion. Finally, the multivariant interaction leads to a double shear of the precipitates during superelastic transformation as the formation of different martensite variants leads to shear stresses in different directions leading to plastic deformation. Ma et al. postulated that the finely dispersed γ′-precipitates in FeNiCoAlTa SMAs may transform within the martensitic matrix when they are small enough [12,13].

In general, it is probable that all these mechanisms occur simultaneously. Fig. 10 schematically illustrates the possible interaction between precipitates and evolving martensite variants. The initial condition shows a fcc parent matrix with dispersed particles (Fig. 10a). If the macroscopic strain is accomplished by a single martensite variant, the precipitate is supposed to undergo an elastic deformation (Fig. 10b). Considering a multivariant accomplishment of the macroscopic strain, the precipitate might be exposed to a double shear stress resulting from two interacting martensite variants (Fig. 10c), which results in an increased friction at the precipitate–martensite interphases leading to a substantial dislocation pile-up in the vicinity of the precipitate capable of stabilizing the martensite (Fig. 10d). In any case, the precipitates provide nucleation zones where martensite starts to evolve. By activating a second or third martensite variant crossbreeding the first one, the shear stresses may increase significantly when encountering the precipitate and this may exceed the matrix strength, leading to irreversible distortion and plastic deformation. Upon further

cycling, this effect is amplified and further contributes to cyclic degradation.

3.4. Summary and conclusions

In the present study, the cyclic deformation behavior of [001]-oriented FeNiCoAlTa single crystals was investigated. In situ microscopy combined with superelastic mechanical cycling revealed a pronounced defect generation at the austenite–martensite and precipitate–martensite phase boundaries, macroscopically manifested in strain accumulation in the stress–strain response. Detailed TEM investigations provided a basis for a model capturing the cyclic degradation mechanism in FeNiCoAlTa shape memory alloys. The current findings can be summarized as follows:

1. Superelastic cycling of [001]-oriented FeNiCoAlTa SMA resulted in substantial accumulation of permanent strain, a distinct shake-down in σ_{crit} for the stress-induced martensite transformation, and a decrease in stress hysteresis within 100 superelastic cycles with a maximum total strain of 4.5%.
2. Detailed in situ optical microscopy showed that multi-variant activation is prevalent, which results in considerable distortions at the interfaces of the interacting martensite variants. This in turn causes local permanent strain accumulation. The local defect generation was found to be responsible for the observed macroscopic cyclic degradation.
3. Detailed TEM investigations provided a basis for a micro-structural explanation of the observed cyclic degra-dation. The results show that the multivariant activation led to an interlocked microstructure with a high volume fraction of retained martensite pinned by dislocation pile ups due to internal friction at the variant interfaces.
4. Finely dispersed γ'-precipitates were found to exhibit a significant amount of retained martensite in the vicinity of the precipitate–matrix interface. This provides for a second mechanism leading to a decrease in the cyclic stability.

Acknowledgements

References

[1] Maki T. In: Otsuka K, Wayman CM, editors. Shape memory materials. Cambridge: Cambridge University Press; 1998. p. 117.
[2] Maki T, Kobayashi K, Minato M, Tamura I. Scr Metall 1984;18:1105.
[3] Omori T, Ando K, Okano M, Xu X, Tanaka Y, Ohnuma I, et al. Science 2011;68:333.
[4] Hayashi R, Murray SJ, Marioni SM, O'Handley RC. Sens Actuators 2000;81:219.
[5] Tanaka Y, Himuro Y, Omori T, Sutou Y, Kainuma R, Ishida K. Mater Sci Eng A 2006;438–440:1030.
[6] Sehitoglu H, Karaman I, Zhang XY, Chumlyakov Y, Maier HJ. Scr Mater 2001;44:779.
[7] Tanaka Y, Himuro Y, Kainuma R, Sutou Y, Omori T, Ishida K. Science 2010;327:1488.
[8] Kireeva IV, Chumlyakov YuI, Kirillov VA, Kretinina IV, Danil'son YuN, Karaman I, et al. Russ Phys J 2011;53:10.
[9] Kireeva IV, Chumlyakov YuI, Kirillov VA, Karaman I, Cesari E. Tech Phys Lett 2011;37:5.
[10] Sehitoglu H, Zhang XY, Kotil T, Canadinc D, Chumlyakov Y, Maier HJ. Metall Mater Trans A 2002;33A:3661.
[11] Chumlyakov YuI, Kireeva IV, Panchenko EYu, Zakharova EG, Kirillov VA. Dokl Phys 2004;49:1.
[12] Ma J, Kockar B, Evirgen A, Karaman I, Luo ZP, Chumlyakov Y. Acta Mater 2012;60:2186.
[13] Ma J, Hornbuckle BC, Karaman I, Thompson GB, Luo ZP, Chumlyakov Y. Acta Mater 2013;61:3445.
[14] Evirgen A, Ma J, Karaman I, Luo ZP, Chumlyakov Y. Scr Mater 2012;67:475.
[15] Geng Y, Jin M, Ren W, Zhang W, Jin X. J Alloys Compd 2012;577:631.
[16] Krooß P, Niendorf T, Karaman I, Chumlyakov Y, Maier HJ. Funct Mater Lett 2012;5:4.
[17] Krooß P, Holzweißig M, Niendorf T, Somsen C, Schaper M, Chumlyakov Y, et al. Scr Mater 2014;81:28.
[18] Gall K, Maier HJ. Acta Mater 2002;50:4643.
[19] Gall K, Sehitoglu H, Anderson R, Karaman I, Chumlyakov Y, Kireeva I. Mater Sci Eng A 2001;317:85.
[20] Gall K, Sehitoglu H, Chumlyakov Y, Kireeva I. Scr Mater 1999;40:7.
[21] Gall K, Sehitoglu H, Chumlyakov Y, Kireeva I. Acta Mater 1999;47:1203.
[22] Simon T, Kroeger A, Somsen C, Dlouhy A, Eggeler G. Acta Mater 2010;58:1850.
[23] Zhang J, Somsen C, Simon T, Ding X, Hou S, Ren S, et al. Acta Mater 2012;60:1999.
[24] Delville R, Malard B, Pilch J, Sittner P, Schryvers D. Int J Plast 2011;27:282.
[25] Kockar B, Karaman I, Kim JI, Chumlyakov YI, Sharp J, Yu CJ. Acta Mater 2008;56:3630.
[26] Sehitoglu H, Karaman I, Anderson R, Zhang X, Gall K, Maier HJ, et al. Acta Mater 2000;48:3311.
[27] Chumlyakov YuI, Kireeva IV, Kretinina IV, Kirillov VA. Russ Phys J 2013;55:11.
[28] Dadda J, Maier HJ, Karaman I, Chumlyakov Y. Int J Mat Res 2010;101:1503.
[29] Stroz D, Chrobak D. Mater Trans 2011;52:358.
[30] Dadda J, Maier HJ, Karaman I, Karaca HE, Chumlyakov YI. Scr Mater 2006;55:663.
[31] Dadda J, Canadinc D, Maier HJ, Karaman I, Karaca HE, Chumlyakov YI. Philos Mag 2007;87:2313.
[32] Dadda J, Maier HJ, Niklasch D, Karaman I, Karaca HE, Chumlyakov YI. Metall Mater Trans A 2008;16:1006.
[33] El-Awady J, Woodward C, Dimiduk D, Ghoniem N. Phys Rev B 2009;80:10.
[34] Dlouhy A, Khalil-Allafi J, Eggeler G. Philos Mag 2003;83:339.